Temperature- and gate-tunable helicity-dependent photocurrent in Dirac semimetal Cd_3As_2 nanobelts

Bob Minyu Wang, Renzhi Sun, Ziyi Song, and Dong Yu*
Department of Physics and Astronomy, University of California, Davis, California 95616, USA

(Received 28 March 2024; accepted 6 June 2024; published 18 June 2024)

Recently, we have demonstrated helicity-dependent photocurrent (HDPC) in strain-free Dirac semimetal Cd_3As_2 nanobelts at room temperature. Here, we investigate their photocurrent response and the photon-helicity modulation at various temperatures and gate voltages. Field effect transistors composed of Cd_3As_2 nanobelts exhibit electron mobility as high as 1.8 m^2/Vs at 13 K with Ohmic contacts achieved by Ar^+ plasma etching. Light exposure to a device at low temperatures substantially reduces its conductivity, likely due to light induced charge trapping. The HDPC is tuned by a factor of 3 as the device is cooled from 200 to 13 K. The solid-state back gating modulates the HDPC by about 25% at 13 K, limited by the persistent negative photoconductance. In contrast, the HDPC magnitude can be enhanced two times by the ionic-liquid gating at room temperature. The symmetry analysis excludes the possibility of the circular photon drag effect and supports the circular photogalvanic effect as the origin of the observed HDPC. We also discuss the temperature and gate dependence based on several interplaying factors including channel resistance, carrier recombination and diffusion, spin relaxation and diffusion, as well as band bending at the junctions.

DOI: 10.1103/PhysRevB.109.245305

I. INTRODUCTION

The past decade or two have been witness to an exciting advancement in electronic materials based on topology. The unique surface states in these materials exhibit symmetry protected electron transport highways with momentum strongly coupled to spin [1–4]. However, the study of these surface states is often convoluted by the bulk states as most topological materials are either metallic or have narrow bandgaps [5]. Shrinking the crystal size down to the nanometer regime can mitigate the bulk interaction because of their large surface-to-volume ratios. Field effect transistors (FETs) made of nanometer-thin materials also enable more efficient gate tunability [6], greatly facilitating the scientific investigation of the topological surface states, as well as providing ideal platforms for potential electronic applications [7,8]. The nontrivial topology in these materials also enables efficient spin generation [9,10]. Spin generation and manipulation via circularly polarized light has been recently demonstrated in topological insulators [11–13] as well as Weyl semimetals [14].

Cd_3As_2 is a prototypical topological Dirac semimetal (DSM), with high carrier mobility and relatively high chemical stability. Though the centrosymmetric Cd_3As_2 crystal possesses chirality-degenerate Weyl cones, spin polarization can be induced by helical photons at its surface where the inversion symmetry is broken. Indeed, we have recently demonstrated unambiguous signatures of helicity-dependent photocurrent (HDPC) in Cd_3As_2 nanobelt FETs at room temperature [15]. Here, we report temperature and gate dependent HDPC in these devices. We show that the degree of helicity dependence is substantially enhanced at lower temperatures and the gate can also effectively tune the magnitude of the HDPC. Rigorous symmetry analysis is also carried out to clarify the mechanism of the HDPC generation.

II. METHODS

A. Synthesis and device fabrication

Our Cd_3As_2 nanobelts were grown by chemical vapor deposition following a recipe adapted from previous reports [16–18]. Briefly, Cd_3As_2 lumps and powder (99% purity, Alfa Aesar) were first placed 10-cm upstream from the center of a quartz tube within a Lindberg tube furnace. The furnace was ramped to 640 °C and held for 15 min. Ar gas flowing at 20–30 sccm carried vapor 15 cm downstream to a Si substrate where deposition occurred at 200–250 °C. The Si substrate was elevated to the center of the tube using a quartz platform. The furnace was naturally cooled to 500 °C when the gas was switched off and the chamber was evacuated. The furnace was finally left to cool to room temperature in vacuum.

The resulting free-standing nanobelts were then mechanically transferred to 300 nm SiO_2 covered Si chips by gently stamping the Si chip onto the as-grown substrate. FETs incorporating single nanobelts were fabricated by standard e-beam lithography (EBL, FEI 430 NanoSem) with 5-nm Cr/295-nm Au deposited as contacts. Two separate methods of deposition were performed. The first was standard e-beam evaporation with no pretreatment. The second was a sputtering process (Lesker Labline Sputter System, 100 W, 15 min, 10 mTorr) preceded by *in situ* Ar^+ plasma etching (65 W, 5 min, 10 mTorr) to eliminate the native oxide layer.

*Contact author: yu@physics.ucdavis.edu

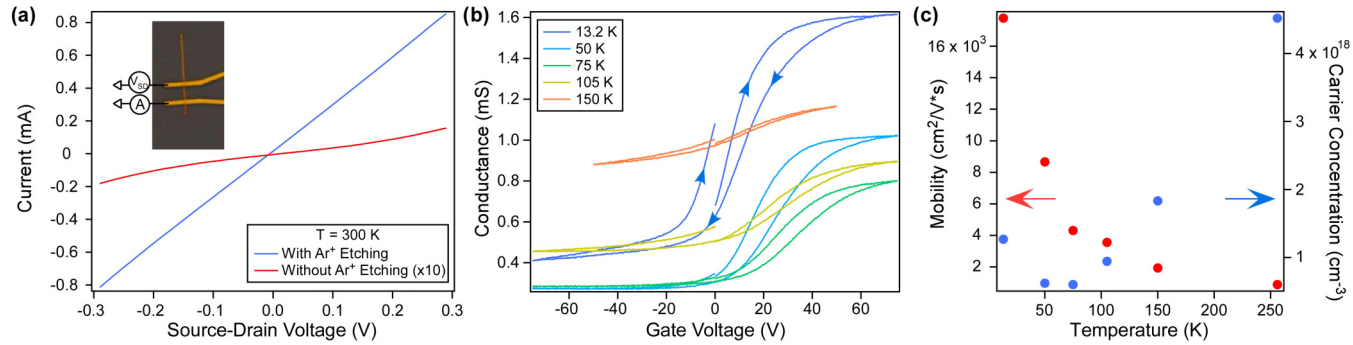

FIG. 1. Cd_3As_2 nanobelt FET characteristics in Device #1. (a) Source-drain characteristics with and without employing Ar^+ plasma etching. Inset: Optical image of Device #1. (b) Conductance vs gate voltage at various temperatures of an plasma etched device. Arrows denote the direction of the gate sweep. (c) Field-effect carrier mobility (red) and electron concentration (blue) extracted from the transconductance in (b).

B. Circularly polarized photocurrent measurements

Spatially resolved photocurrent measurements were performed using a 532-nm continuous wave laser focused by a 10× N.A. 0.30 objective lens. Photocurrent images were obtained by raster scanning the focused laser on the device plane using a pair of mirrors mounted on galvanometers. Photocurrents were measured as a function of laser position and photon polarization through a DL1211 preamplifier followed by a LabView data acquisition board. Low temperature measurements were performed in a Janis ST-500 optical cryostat with a tilted sample stage for oblique incidence. The laser beam was transversely incident to the channel at an angle of $\theta = 45^\circ$. Circular polarization of light was achieved by passing a linearly polarized beam through a rotating zero-order quarter wave plate (QWP) at 532 nm (Thorlabs). Photocurrent maps were taken at zero source-drain bias in discrete steps of QWP rotation. The photocurrent as a function of the QWP angle at each pixel was then fit to extract parameters to construct the HDPC map. More details are provided in Ref. [15].

C. Ionic liquid gating

After the complete fabrication of a nanobelt FET, a 450-nm-thick poly(methyl methacrylate) (PMMA 950, C4, MicroChem) layer was spin coated at 4000 rpm for 40 sec on top of the device, followed by baking at 160 °C for 5 min. Then a second EBL was performed, followed by development to partially remove PMMA and expose the gate electrode and only a part of the nanobelt. Finally, a droplet of polyethylene glycol (PEO, MW = 1000, Alfa Aesar) with 5 wt. % $NaClO_4$ (Alfa Aesar, 98%) was applied to the nanobelt device. By controlling the amount of PEO applied to the tip of a microfiber, we achieved a small liquid droplet with a size of 100 μm to minimize leak current. The gate leak current was substantially smaller than the photocurrent in all measurements.

III. RESULTS

A. Field effect transistor characteristics

Devices were fabricated both with and without *in situ* Ar^+ plasma etching prior to contact deposition. Of these devices, only the etched devices exhibited Ohmic contacts as shown by a linear I-V dependence in Fig. 1(a). The nonlinearity in devices that were not etched is likely due to the presence of a surface CdO_x layer which functions as a tunneling barrier [19]. The Ar^+ plasma etching treatment presumably removed the oxide layer. The resistance is 56 times smaller in the etched device as shown in Fig. 1(a). The contact resistance measured in four-probe devices decreases from 10–100 kΩ to about 100 Ω after etching, only a fraction of the channel resistance.

The electron mobility (μ) was extracted from field effect measurements in an Ohmic device taken at various temperatures [Fig. 1(b)]. The saturation of gate dependence at both positive and negative V_g as seen in Fig. 1(b) has been previously reported [20,21] and was attributed to electronic screening as the Fermi level is tuned away from the Dirac point. The steepest region of the linear regime as shown in Fig. 1(b) was fit for the extraction. The mobility was calculated by $\mu = \frac{dI_{DS}}{dV_g}\frac{t_{ox}L}{\epsilon_{ox}\epsilon_0 W V_b}$, where $\frac{dI_{DS}}{dV_g}$ is the transconductance, t_{ox} is the oxide thickness, L is the channel length, W is the channel width, ϵ_{ox} is the oxide dielectric constant, ϵ_0 is the permittivity in vacuum, and V_b is the source-drain bias. The carrier concentration was assumed to be uniform over the nanobelt with a thickness of 100 nm. μ reached as high as 1.8 × 10^4 cm^2/Vs at 13 K. We found that μ drastically increases by more than a factor of 10 from 78 K to 13 K. Previous studies of thin Cd_3As_2 suggest that the rise of μ tapers out under 100 K [6,18]. However, μ in our devices continues to rise below 100 K. In fact, it increases more drastically at lower temperatures. The difference may be caused by the more Ohmic contact or lower defects in our devices. The relatively large hysteresis at low temperatures was caused by accidental exposure of devices to weak photoexcitation of room light about a few mW/cm^2 (see next section).

B. Negative photoconductance

The Cd_3As_2 nanobelt devices exhibit negative photoconductance (NPC) (Fig. 2), which has been reported in multiple nanostructures, such as InAs nanowires [22], Si nanowires [23], and Cd_3As_2 nanowires [18]. Its origin has been attributed to the trapping of charge carriers in the surface defect states, which suppresses the mobility or the density of the conduction charge carriers. The previous work on the NPC in Cd_3As_2 nanowires [18] was carried out only at

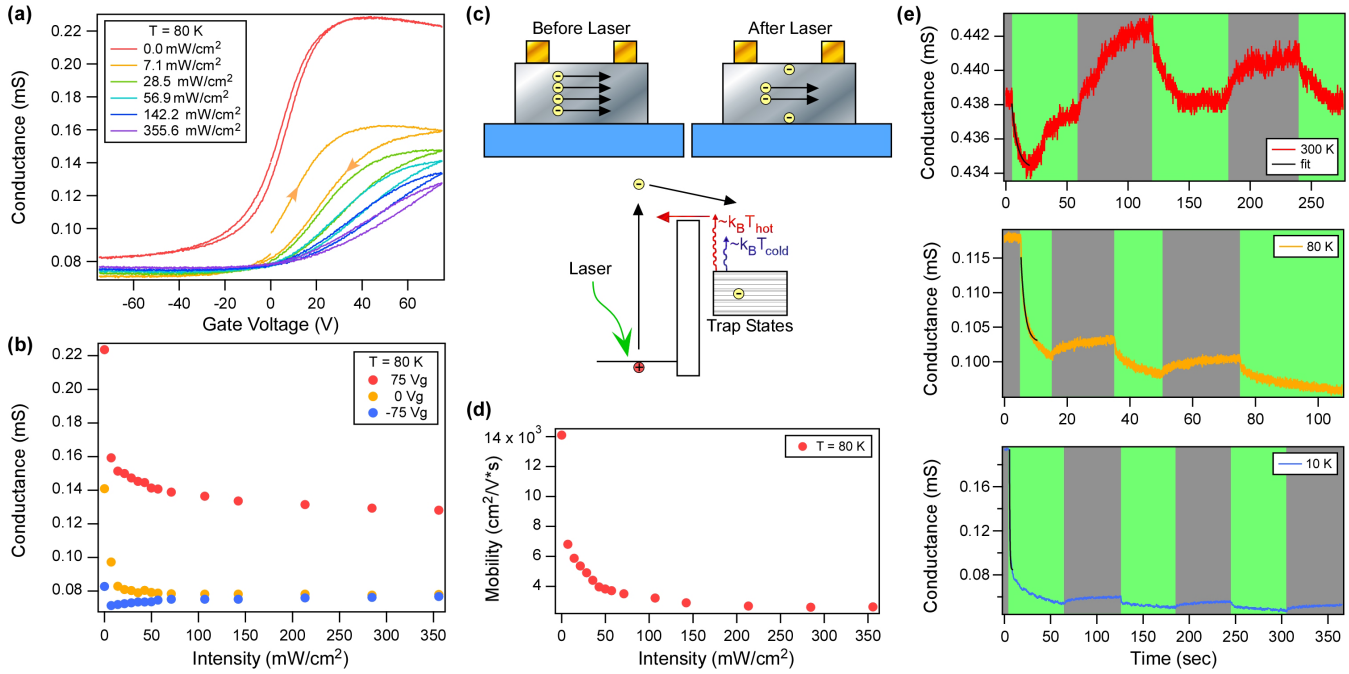

FIG. 2. Negative photoconductance in Cd_3As_2 nanobelt FETs measured in Device #2. (a) Gate dependent conductance under photoexcitation of various intensities at 80 K. The gate voltage is scanned at 1.25 V/s. (b) Conductance extracted at representative gate voltages as a function of incident intensity. (c) Schematic depicting the effect of surface traps on the gate response of Cd_3As_2 nanobelt FETs under illumination (upper). Diagram depicting the energy barriers and relaxation pathways of photogenerated electrons. Trapped electrons are more likely to escape at higher temperatures, represented by the red arrow over the energy barrier. (d) Field effect carrier mobility as extracted from the steepest slope as a function of light intensity. (e) Conductance time trace at different temperatures as light is switched on (green) and off (grey). Light intensity was 1420 mW/cm^2 at 300 K and 284 mW/cm^2 at both 80 and 10 K. The black curves are exponential fittings to the initial drop in conductance upon light exposure.

room temperature. As the NPC behaviors are important to understanding the temperature and gate dependent HDPC, we performed a systematic temperature-dependent NPC study.

At 80 K, as the light intensity increases, the slope of the gate dependent conductance decreases. This indicates a lower mobility, likely caused by the scattering of the trapped charges [Figs. 2(a) and 2(d)]. The gate voltage threshold for the onset of the rise in conductance appears to shift in the positive direction at higher intensity. This implies that the light exposure leads to electron trapping, which acts as a local gate and causes the originally *n*-type device to become more *p*-type. As a result, a more positive gate voltage is needed to turn on the device. A large hysteresis in the gate scan is observed under light, reflecting a slow trapping process. Conductance is reduced by almost half under photoexcitation of just a few mW/cm^2, but the reduction is saturated at higher intensity [Fig. 2(b)], presumably because most traps are filled. The conductance increases with light intensity at $V_g = -75$ V, but decreases with light intensity at $V_g = 0$ and 75 V as shown in Fig. 2(b). This is because the device shows ambipolar conduction and becomes slightly p type at large negative gate voltage. The light exposure leads to electron trapping, which increases the hole density and the conductance in the *p*-type regime, while decreasing the electron density and the conductance in the *n*-type regime. At low temperatures, the light induced reduction in conductance persists even after the light is removed [Fig. 2(e)]. Both the conductance reduction percentage and the recovery time significantly increase at low temperatures. The conductivity is reduced by a factor of 4 after light exposure at 13 K. Below 80 K, the device stays in the low conductance state for hours after light exposure. The device conductance can be recovered after warming to higher temperatures. The conductance only changes by 1% upon light exposure at room temperature. Different from the low temperature data, conductance drops and then increases in the first cycle of light exposure [Fig. 2(e)]. We suspect that this initial baseline shift may be caused by the slight temperature change as the device was warmed to room temperature right before the measurement.

C. Temperature dependent HDPC

The spatial distribution of HDPC agrees with the spin-momentum locking mechanism and has been previously reported in detail [15]. Here we focus on the temperature and gate dependent HDPC with laser focused near the contacts. HDPC measurements were performed with the laser beam focused to a diameter about 2.5 μm close to the contact connected to the pre-amplifier. The photocurrent in the vicinity of the contact differs under left and right circular polarizations [Fig. 3(a)] and can be fit well by the following equation:

$$I = C\sin(2\alpha) + L_1\sin(4\alpha) + L_2\cos(4\alpha) + D, \quad (1)$$

where α is the angle between the QWP fast axis and the incident linear polarization, C represents the amplitude of the HDPC, L_1 is the linear polarization-dependent effects, L_2 is

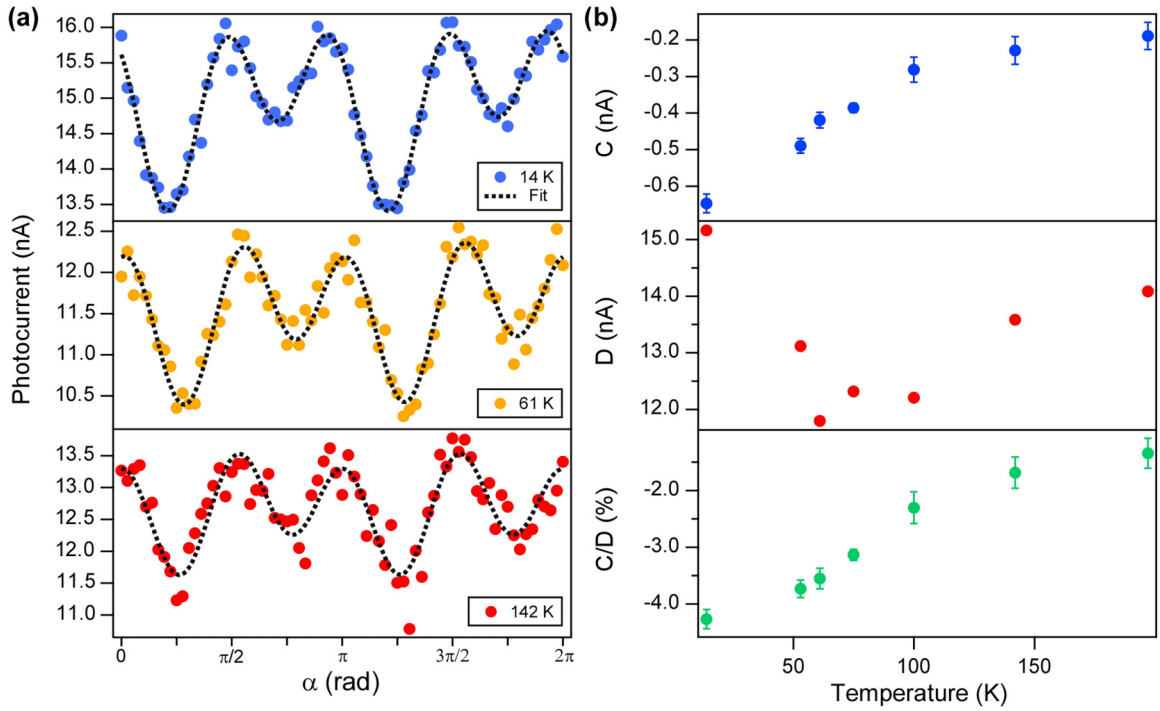

FIG. 3. Temperature dependent HDPC measured in Device #1. (a) Photocurrent measured with the laser focused close to the current-collecting contact as a function of α. The dashed lines represent the fit used to extract the parameters in (b). (b) Extracted C, D, and C/D as a function of temperature. A CW laser of 532 nm with peak intensity of 326 W/cm^2 was used at each temperature.

the reflectance difference at s and p polarizations, and D is the polarization-independent component.

As the temperature decreases, the magnitude of C monotonically increases, first slowly and then more quickly [Fig. 3(b)]. $|C|$ increases by more than a factor of 3 as the temperature decreases from 200 to 14 K. In contrast, D first decreases at lower temperatures, reaching a minimum at about 70 K, and then increases again. Its overall change is about 20%, much smaller compared to C. Importantly, the temperature dependence of C and D follows distinct trends, indicating different generation mechanisms. The $|C/D|$ ratio increases from 1.3% to 4.3% as the temperature decreases from 200 K to 14 K, reflecting a larger degree of spin polarization at lower temperatures. As the device is necessarily exposed to photoexcitation when the HDPC is measured, the significant NPC effect at low temperatures can reduce the electron mobility and concentration, potentially suppressing the HDPC.

D. Solid-state gating dependent HDPC

The HDPC measured with the laser focused near the contact can be tuned by a back-gate voltage applied to the Si substrate with a 300-nm SiO_2 dielectric layer. At 13 K, $|C|$ stays about the same in the negative V_g, but increases by about 25% at positive V_g [Fig. 4(c)]. This is similar to the gate-induced conductance change after the light exposure [Fig. 2(a)]. D follows a similar trend as well, but it increases more than C, by about 40% [Fig. 4(b)]. The devices exhibit qualitatively similar behavior at slightly higher temperatures up to 150 K, albeit at a smaller extent than at 13 K. Again, the light exposure needed for the HDPC measurements significantly reduce the gate tunability of the HDPC at low temperatures.

E. Ionic-liquid gating dependent HDPC

Compared to solid-state gating, ionic-liquid gating provides a more efficient way to tune carrier concentration by forming an electric double layer or by electrochemical doping at the surface. Electrolyte gating with ionic liquids has been employed to induce metal-insulator phase transitions [24,25] and superconductivity [26]. This technique has recently been applied to Cd_3As_2 [27] but the study focused on gate tunable quantum oscillations. Here we demonstrate that this method can be used to induce and tune the HDPC in the Cd_3As_2 nanobelts at arbitrary locations away from the metal contacts at room temperature. Figure 5(a) shows the device configuration, where the nanobelt device is partially covered by PMMA. A window is opened by a second e-beam lithography step to expose a segment of the nanobelt to the electrolyte solution composed of $NaClO_4$ in PEO. Optical images of devices before and after depositing PEO can be found in Fig. 6. The PMMA layer effectively blocks the ions from entering the covered nanobelt as we have demonstrated previously [25]. Upon applying positive voltage to the gate electrode immersed in the electrolyte, Na^+ ions form an electrical double layer which then applies a large external vertical electric field only on the exposed part of the channel. Consequently, the electron concentration in the exposed segment increases substantially. As a rough estimation, the ionic liquid gating induced carrier concentration change can be estimated by $n_{IL} = \epsilon_{IL}\epsilon_0 V_g/d_{dl}d_{nr} = 10^{18}$ cm^{-3}, where we assumed the

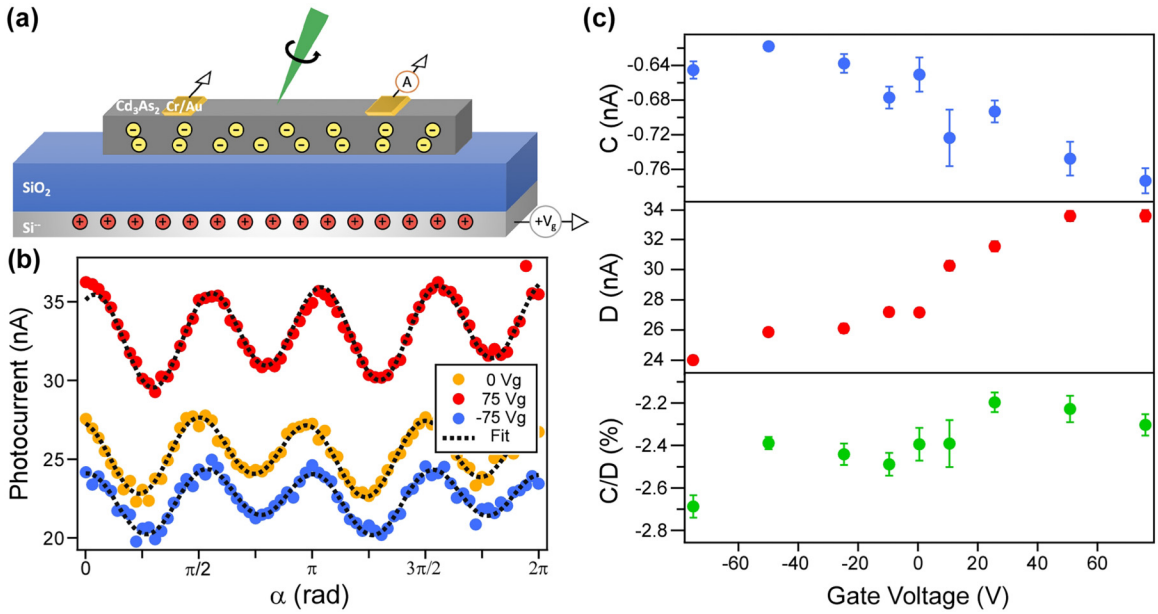

FIG. 4. Back-gate dependent HDPC measured in Device #1 at 13 K. (a) Schematic of the effect of back gate voltage on the carrier concentration during the HDPC measurement. (b) Photocurrent measured with the laser focused close to the current-collecting contact as a function of α, at representative gate voltages. The dotted lines depict the fits used to extract the parameters in (c). (c) Extracted C, D, and C/D as a function of gate voltage.

ionic liquid dielectric function $\epsilon_{IL} = 2$ and the double layer thickness $d_{dl} = 0.6$ nm, $V_g = 0.7$ V, and the carriers are uniformly distributed across the thickness in the nanoribbon $d_{nr} = 100$ nm. As the electron concentration outside of the window is unaffected, a doping gradient with a sharp boundary is developed, creating strong band bending and in plane electric fields near the window edge.

The PEO solution remains in the liquid phase at room temperature and is optically transparent (Fig. 6), allowing photocurrent imaging. The photocurrent is absent at the window edges before the electrolyte deposition. After the application of PEO, a small photocurrent can be seen already at the window edges even before a gate voltage is applied. Under $V_g = 0.7$ V, photocurrent spots of opposite polarities

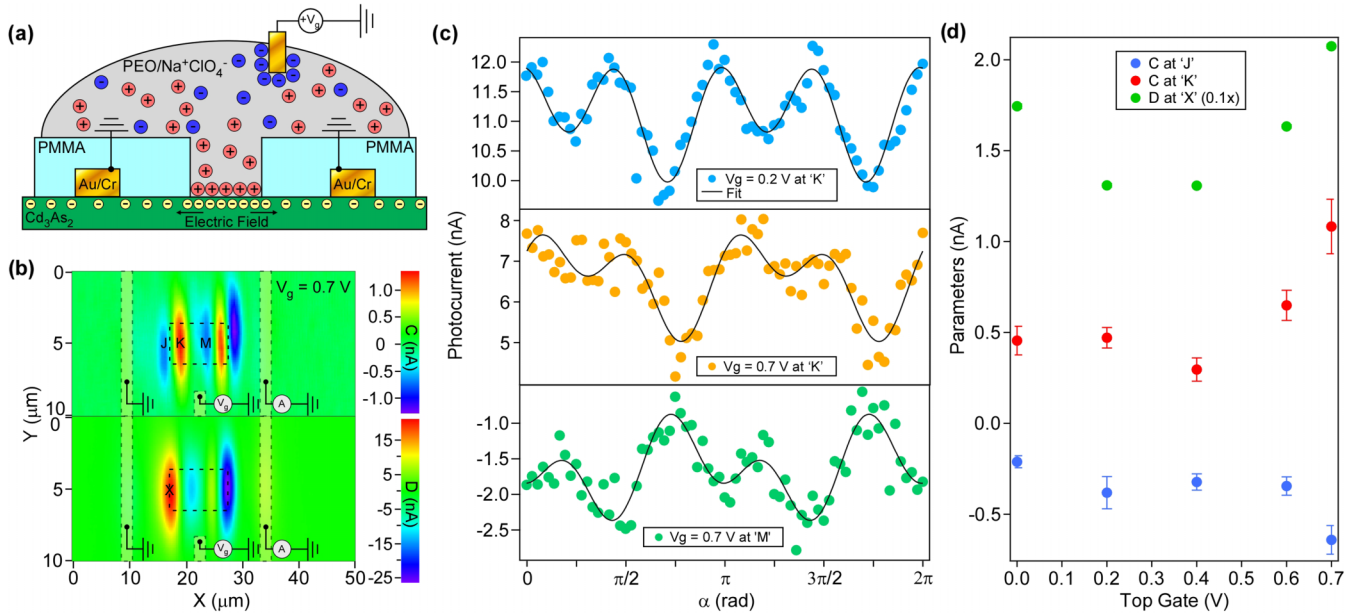

FIG. 5. Ionic liquid top-gate dependent HDPC measured in Device #3 at 300 K. (a) Schematic of the ionic-liquid gate configuration. (b) Helicity dependent (upper) and independent (lower) photocurrent map of the device while applying a 0.7 V gate voltage. (c) Photocurrent at positions K and M in (b) as a function of α at different top-gate voltages. The black curves are the fits used to extract the parameters in (d). (d) C and D extracted from the fits in (c). C is extracted from positions J and K while D is extracted from position X in (b).

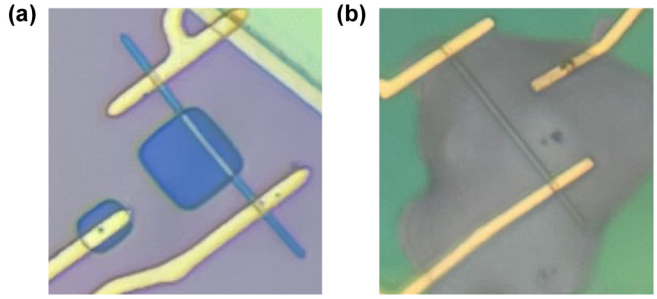

FIG. 6. Optical images of representative devices at different stages of the fabrication cycle. (a) A representative device after the coating of PMMA and its partial removal. The purple area is covered by PMMA. The blue squares are areas where PMMA are removed by EBL and developing to expose the nanobelt for potential ionic-liquid gating. (b) Device #3 after applying PEO. Note that once PEO was applied, the window cannot be seen optically because of the matching index of refraction of PEO and PMMA.

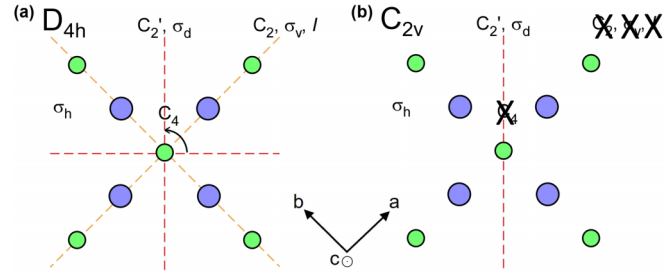

FIG. 7. Schematic depicting crystal symmetry in Cd_3As_2. Purple circles represent Cd ions while green circles represent As ions. (a) is for the bulk with D_{4h} symmetry and (b) is for the {110} surface with C_{2v} symmetry. Note that the a and b crystallographic axes are collinear with the rotation axes along the atoms. The dashed lines represent the mirror planes. σ_h is the mirror plane parallel to the page.

are clearly observed near the edges of the window [D map in Fig. 5(b)], indicating the ionic-liquid gating-induced doping gradient. The photocurrent at the window edges dominates over that at the contact interfaces, implying the ionic-liquid gating induces much stronger band bending than the Schottky contacts do. Clear helicity dependence can be observed near the window edges as shown in Fig. 5(c). Similar to the spatial profile of the HDPC around the contacts, C has the same sign at opposite edges within the window, and switches sign outside of the window [Fig. 5(b)], consistent with the spin-momentum locking mechanism [15]. An additional photocurrent peak is shown in the C map at about $x = 25$ μm (position M) [Fig. 5(b)]. Equation (1) also fits well at this location, suggesting that the HDPC is observed in the middle of the ionic-liquid gated channel. $|C|$ is enhanced by about a factor of two as the ionic-liquid gate voltage increases from 0 to 0.7 V [Fig. 5(d)]. Pushing the gate voltage farther positively or negatively tends to irreversibly damage the devices.

IV. DISCUSSION

We first discuss the possible mechanisms for the observed HDPC in our Cd_3As_2 devices through symmetry analysis, where we focus on analyzing the circular photogalvanic effect (CPGE) and the circular photon drag effect (CPDE) in bulk and at surface. Then we discuss the temperature and gate dependent HDPC.

A. Photocurrent symmetry analysis in Cd_3As_2

To analyze the HDPC ($\vec{J}^{HDPC}$) generated by the optical field ($\vec{E}$), we start with a general expression [28],

$$\begin{aligned} J_\lambda^{HDPC} &= J_\lambda^{CPGE} + J_\lambda^{CPDE} \\ &= \gamma_{\lambda\mu} i(\vec{E} \times \vec{E}^*)_\mu + T_{\lambda\delta\mu} q_\delta (\vec{E} \times \vec{E}^*)_\mu, \end{aligned} \tag{2}$$

where $\gamma_{\lambda\mu}$ is a second-rank tensor, $T_{\lambda\delta\mu}$ is a third-rank tensor, $\vec{q}$ is the photon wave vector, and the indices run through three spatial coordinates. The first term represents the CPGE and the second CPDE. Note we dropped the linear photogalvanic and linear photon drag terms in the above expression as we want to focus on analyzing circular polarization dependence. We will discuss the CPGE and CPDE terms separately below, where the symmetry analysis predicted dependence on the azimuthal and polar angle of incidence is compared to the experimental results to distinguish J^{CPGE} from J^{CPDE}.

Symmetry analysis for CPGE. Because J_λ^{CPGE} changes sign upon spatial inversion while the square of the electric field does not, $\gamma_{\lambda\mu}$ has nonzero components only for systems lacking inversion symmetry. It is now generally accepted that the Cd_3As_2 crystal has inversion symmetry [space group $I4_1/acd$ and point group D_{4h} depicted in Fig. 7(a)] and hence the CPGE is not allowed in the bulk of the material.

However, the top surface of the nanobelt belongs to a different point group than the bulk. The surface index is {110} as shown in Ref. [15]. The C_4 rotation symmetry and some of the mirror planes are removed at the surface as shown in Fig. 7(b). In this orientation, the c or [001] crystallographic axis points along the x axis in the surface, making the original bulk C_2' rotation axis now normal to the surface as the z axis. In addition, the vertical mirror planes σ_d and σ_h are preserved on the surface. These operators generate the C_{2v} point group. The second-rank tensor describing J^{CPGE} in the C_{2v} point group is [29]:

$$\gamma_{C_{2v}}(\omega) = \begin{pmatrix} 0 & \gamma_{xy}(\omega) & 0 \\ \gamma_{yx}(\omega) & 0 & 0 \\ 0 & 0 & 0 \end{pmatrix}. \tag{3}$$

Plugging this into Eq. (2), we have

$$\begin{aligned} J_x^{CPGE} &= i\gamma_{xy}(\vec{E} \times \vec{E}^*)_y, \\ J_y^{CPGE} &= i\gamma_{yx}(\vec{E} \times \vec{E}^*)_x. \end{aligned} \tag{4}$$

The components of $(\vec{E} \times \vec{E}^*)$ incident on the device are given by

$$\begin{pmatrix} (\vec{E} \times \vec{E}^*)_x \\ (\vec{E} \times \vec{E}^*)_y \\ (\vec{E} \times \vec{E}^*)_z \end{pmatrix} = \begin{pmatrix} -2i\sin(2\alpha)\sin(\theta)\cos(\phi)E_0^2 \\ -2i\sin(2\alpha)\sin(\theta)\sin(\phi)E_0^2 \\ -2i\sin(2\alpha)\cos(\theta)E_0^2 \end{pmatrix}, \tag{5}$$

where θ is the polar angle between the surface normal axis and the light propagation vector, and ϕ is the azimuthal angle within the surface plane. The explicit incident angle

dependence of J^{CPGE} is then

$$J_x^{CPGE} \propto \sin(2\alpha)\sin(\theta)\sin(\phi),$$
$$J_y^{CPGE} \propto \sin(2\alpha)\sin(\theta)\cos(\phi). \quad (6)$$

The above angular dependence is consistent with our experimental observation (incident angle dependence experimental results can be found in our previous work [15]), indicating the observed HDPC is likely originated from the surface where the symmetry is reduced from D_{4h} to C_{2v}.

Symmetry analysis for CPDE: The CPDE relies on the momentum transfer from incident photons to electrons and is a higher order effect [30]. As a result, the CPDE does not require a broken inversion symmetry to manifest HDPC like the CPGE does, and has been observed in centrosymmetric graphene monolayers [30,31], and potentially in monolayer $MoSe_2$ [32]. To evaluate the possible CPDE contribution, we performed symmetry analysis for the CPDE partially following the work in Ref. [32], though we focused on the relevant D_{4h} and C_{2v} point groups here. We show in the Appendix, through detailed symmetry analysis, that the CPDE is not allowed in the bulk. Furthermore, the {110} surface with C_{2v} symmetry exhibits CPDE current with incidence longitudinal to the channel, inconsistent with our experimental observation. Therefore, we exclude the possibility of the CPDE contribution to our observed HDPC.

B. Temperature and gate dependent HDPC

As shown in the experimental results, both helicity independent (D) and dependent (C) photocurrent components vary with temperature and gate voltage. The local circularly polarized photoexcitation creates an electromotive force (EMF) and the measured photocurrent is given by this EMF divided by the channel resistance. Hence, both D and C can be affected by the channel resistance, which is a function of temperature and gate voltage. However, D and C have different physical origins: D is created by the junction electric potential gradient, while C is created by the spin-momentum locking as a result of topological surface states.

As detailed in our previous work [15], the circularly polarized light induces spin polarization at the top surface of an optically thick DSM slab, leading to unbalanced momentum and the observed HDPC. The circularly polarized laser focused anywhere in the channel should drive a local EMF. However, such an EMF in the middle of channel does not produce measurable photocurrent, because of the local current dissipation through the parallel path of the conductive Cd_3As_2 bulk. Only when the spin injection is close to the contact does the contact band bending suppress the current dissipation through the bulk. Therefore, there are two requirements for creating HDPC in DSMs: (1) spins are injected into states with spin-momentum coupling; (2) spins must be injected into an area with large band bending. We discuss below the factors affecting D and C.

D depends on the channel resistance, contact band bending, and carrier diffusion length. Smaller channel resistance and larger contact band bending increase D. At all temperatures, the photocurrent quickly decays as the laser is scanned away from the contact, indicating that the carrier diffusion length is shorter than the laser spot diameter of 2.5 μm. A longer carrier diffusion length then means more photogenerated carriers can arrive at the charge collecting contact, increasing D.

C depends on the channel resistance, spin relaxation time, spin diffusion length, and contact band bending. Smaller channel resistance increases C. Longer spin relaxation time enables larger spin polarization and enhances C. Similar to carrier diffusion length, the longer spin diffusion length allows spin to more effectively diffuse to the contact, which favors the collection of the spin-induced charge current by the contact. A larger band bending means that the spin-induced charge current is less likely to flow out of the depletion region and dissipate through the bulk, enhancing C.

Both temperature and gate voltage can affect these factors. We discuss their effects below.

Temperature dependence. $|C|$ is enhanced at lower temperatures (Fig. 3) as both the spin relaxation time and spin diffusion length increase at lower temperatures. Though the channel resistance also increases at lower temperatures, it is not enough to compete with the other two factors since they likely change much more.

The channel resistance increases and the contact band bending decreases at lower temperatures, both contributing to the decrease in D down to 70 K. However, the increase in D below 70 K suggests a different competing mechanism is at play. One possible mechanism is an increase of the minority carrier diffusion length [33]. The carrier diffusion length is determined by the hole diffusion coefficient D_p and the hole recombination time τ_p, $L_p = \sqrt{D_p\tau_p} = \sqrt{\mu_p k_B T \tau_p/q}$. Figure 1(c) shows that the electron mobility increases by more than four times below 70 K. How exactly the hole mobility changes with temperature is unclear but its potential increase is likely counteracted by a more than five times drop in temperature down to 13 K. Hence, the hole diffusion coefficient is not expected to change much with temperature. On the other hand, the carrier recombination time is expected to increase as a result of suppressed phonon activity at low temperatures, likely causing the rise of photocurrent.

Solid-state gate dependence. The channel resistance decreases by 50% under $V_g = 75$ V, similar to the increase of D, indicating the gate tuning of D is likely caused by the change in the channel resistance. In addition, a positive V_g simultaneously enhances band bending which tends to increase the photocurrent. In the mean time, a positive V_g also increases the electron concentration, which likely reduces the minority carrier lifetime and leads to a reduced minority carrier diffusion length. The effects of increased band bending and reduced diffusion length likely cancel each other, leaving only the change in channel resistance to explain the change in observed photocurrent under a gate voltage.

$|C|$ only increases by about 25% under $V_g = 75$ V, less than that expected from the channel resistance reduction. The reason is unclear but one possible explanation is the reduced spin relaxation time under the positive gate voltage. Spin transport may also be suppressed with shortened Fermi arcs when the Fermi level is shifted away from the Dirac point [4]. Further studies should be conducted to elucidate the underlying mechanism.

The HPDC must be measured under light exposure which generates charge trapping as manifested by the persistent NPC

at low temperatures. The channel resistance is modulated by a factor of 3 by gate in the dark but only up to 50% under light exposure [Fig. 2(a)]. A much higher gate tunability of HDPC is expected if NPC can be suppressed.

NPC and its impact on gate tunable HDPC. We now divert to the NPC effect, to better understand the gate dependence. As shown in Fig. 2(e), at low temperatures, a persistent conductivity suppression is observed even when the photoexcitation is removed. A similar memory behavior has been observed in InAs nanowires [22] and was attributed to the existence of an energy barrier between the trap states and the conduction band. At low temperatures, the trapped carriers do not have sufficient thermal energy to overcome this barrier, leading to a persistent low-conductance state [Fig. 2(c)]. At high temperatures, the thermal energy can assist the detrapping process and enable fast recovery after the photoexcitation. The rate at which this thermally activated detrapping occurs can also be inferred by the time it takes conductance to drop upon initial light exposure. Since trapping occurs in conjunction with detrapping, conductance continually changes over a time scale of seconds before equilibrium is reached. These time constants are extracted by fitting the initial drops in Fig. 2(e) exponentially, dropping from 4.5 s at 300 K, to 1.3 s at 80 K, and then to 0.49 s at 10 K. Faster detrapping at 300 K makes more traps available for a longer period of time before the traps are saturated, whereas the opposite occurs at low temperatures.

This persistent charge trapping also leads to a relatively small gate modulation of C at low temperatures. The laser intensity used for the CPGE measurements is about 300 W/cm^2, much higher than needed to fill available traps. These trapped charges distributed in the conduction channel reduce the gate tunability of both C and D. Better surface passivation may suppress the trap states and mitigate the NPC, which can potentially improve the gate tunability of HDPC.

Ionic-liquid gate dependence. Thanks to the highly efficient ionic gating and the minimal charge trapping at room temperature, the application of an ionic-liquid gate voltage tunes the HDPC by a factor of two, significantly higher than the back gate at low temperatures. The measurements also clearly demonstrate that proximity to the metal contact is not needed to generate HDPC. Instead, HDPC can be switched on at any point in the channel where large band bending is created by ionic-liquid gating [Fig. 5(b)], supporting the requirements of HDPC in DSMs as discussed earlier. Both C and D increase in magnitude with increasing ionic-liquid gate voltage [Fig. 5(d)]. The change is unlikely solely caused by the gate-induced channel resistance reduction, since only the ionic-liquid exposed region is affected by the gate voltage and the total channel resistance does not change much. Instead, the C and D increase is more likely caused by the gate-enhanced band bending at the window edge. The initial drop of D at small gate voltage is likely caused by the gate hysteresis, as a gate scan was performed before the photocurrent measurements. The exact origin of the C spot observed in the middle of the gating window is unclear. But it may be caused by the strong surface band bending induced by the ionic gating which suppresses the current dissipation through the bulk.

V. CONCLUSION

In summary, we demonstrate that the HDPC magnitude increases three times in Cd_3As_2 nanobelt FETs as the temperature is decreased from 200 to 13 K. The HDPC is also gate tunable via both solid-state back-gate and ionic-liquid top-gate configurations. The back gate tunes the HDPC by about 25% at 13 K, likely limited by the light-induced charge trapping at low temperatures. The ionic-liquid gating increases the HDPC two times at room temperature. Interestingly, the helicity dependent and independent photocurrent components often have distinct temperature and gate dependence, indicating they are created by different mechanisms. We show that the temperature and gate dependence can be understood by an intricate dance involving changes in carrier density, diffusion and recombination, spin diffusion and relaxation, as well as band bending. We also performed rigorous symmetry analysis entailing the plausibility of CPGE and against CPDE in Cd_3As_2. Our work not only strengthens the fundamental understanding of light polarization controlled spin manipulation in Dirac materials, but also provides a practical method for electrical tuning of helicity-sensitive optoelectronic devices.

ACKNOWLEDGMENTS

We acknowledge P. Klavins for his assistance in setting up and maintaining the helium recovery and liquefaction system. This work was supported by the U.S. National Science Foundation Grants No. DMR-2105161 and No. DMR-2209884. Part of this study was performed at the UC Davis Center for Nano and Micro Manufacturing (CNM2).

APPENDIX: DETAILED SYMMETRY ANALYSIS FOR EXCLUDING CPDE

CPDE analysis for the bulk with D_{4h} symmetry. The circular photon drag effect [second term in Eq. (2)] is described by a higher-order tensor $T_{\lambda\delta\mu}$, which may have nonzero components in centrosymmetric systems such as in the bulk of Cd_3As_2. The matrix elements can be identified by applying the generating symmetry operations of the bulk crystal point group, D_{4h}. These include the C_4 rotation and σ_h horizontal mirror. We will derive the nonzero components by first applying C_4 then σ_h.

The rotation matrix corresponding to C_4 is

$$R = \begin{pmatrix} R_{xx} & R_{xy} & R_{xz} \\ R_{yx} & R_{yy} & R_{yz} \\ R_{zx} & R_{zy} & R_{zz} \end{pmatrix} = \begin{pmatrix} 0 & 1 & 0 \\ -1 & 0 & 0 \\ 0 & 0 & 1 \end{pmatrix}. \tag{A1}$$

The CPDE photocurrent can be expressed as follows:

$$J_\lambda^{CPDE} = T_{\lambda\delta\mu} q_\delta (\vec{E} \times \vec{E}^*)_\mu. \tag{A2}$$

If we apply the C_4 rotation, the photocurrent becomes

$$J_l^{CPDE'} = R_{l\lambda} J_\lambda^{CPDE} = R_{l\lambda} T_{\lambda\delta\mu} q_\delta (\vec{E} \times \vec{E}^*)_\mu. \tag{A3}$$

Alternatively, we can rotate the optical field by C_4 and get the same photocurrent

$$J_l^{CPDE'} = T_{lmn} R_{m\delta} q_\delta R_{n\mu} (\vec{E} \times \vec{E}^*)_\mu. \tag{A4}$$

Since the above two equations are equal, we have,

$$R_{l\lambda}T_{\lambda\delta\mu}q_\delta(\vec{E}\times\vec{E}^*)_\mu = T_{lmn}R_{m\delta}R_{n\mu}q_\delta(\vec{E}\times\vec{E}^*)_\mu. \quad \text{(A5)}$$

Note that the bases made by $q_\delta(\vec{E}\times\vec{E}^*)_\mu$ are not independent because for transverse electromagnetic waves, $\vec{q}$ and $\vec{E}\times\vec{E}^*$ are in the same direction and hence we have,

$$q_\delta(\vec{E}\times\vec{E}^*)_\mu = q_\mu(\vec{E}\times\vec{E}^*)_\delta. \quad \text{(A6)}$$

As a result, for each l, Eq. (A5) contains six rather than nine independent equations (three with $\delta=\mu$ and three with $\delta\neq\mu$) as below:

$$\left\{\begin{array}{c} R_{l\lambda}T_{\lambda\delta\delta} = T_{lmn}R_{m\delta}R_{n\delta}, \\ R_{l\lambda}(T_{\lambda\delta\mu}+T_{\lambda\mu\delta}) = T_{lmn}(R_{m\delta}R_{n\mu}+R_{m\mu}R_{n\delta}). \end{array}\right\} \quad \text{(A7)}$$

After evaluating every case under C_4 rotation, the following null and coupled terms are revealed:

$$\begin{gathered} T_{xyy}=T_{yxx}=T_{xxx}=T_{yyy}=T_{yzz}=T_{xzz}=0, \\ T_{zxx}=T_{zyy}, \\ T_{xxy}+T_{xyx}=T_{yyx}+T_{yxy}=T_{zxy}+T_{zyx}=0, \\ T_{zxz}+T_{zzx}=T_{zyz}+T_{zzy}=0, \\ T_{xzx}+T_{xxz}=T_{yzy}+T_{yyz}, \\ T_{yzx}+T_{yxz}=-(T_{xzy}+T_{xyz}). \end{gathered} \quad \text{(A8)}$$

In addition to C_4, D_{4h} also contains the mirror plane σ_h, defined by the following matrix:

$$M=\begin{pmatrix} M_{xx} & M_{xy} & M_{xz} \\ M_{yx} & M_{yy} & M_{yz} \\ M_{zx} & M_{zy} & M_{zz} \end{pmatrix} = \begin{pmatrix} 1 & 0 & 0 \\ 0 & 1 & 0 \\ 0 & 0 & -1 \end{pmatrix}. \quad \text{(A9)}$$

After applying σ_h to all cases that remain nonzero after applying C_4 using the same analysis as above, we find that all terms become zero. We therefore conclude that CPDE is not allowed for the D_{4h} symmetry.

CPDE analysis for the surface with C_{2v} symmetry. The {110} surface of the Cd_3As_2 crystal has C_{2v} symmetry. This reduced symmetry allows CPDE on the surface of the crystal. We performed the same analysis as above with a C_2' rotation followed by σ_h and σ_d reflections to determine the zero and independent elements of the CPDE tensor.

C_2' rotation is dictated by the following matrix:

$$\begin{pmatrix} \cos(\pi) & \sin(\pi) & 0 \\ -\sin(\pi) & \cos(\pi) & 0 \\ 0 & 0 & 1 \end{pmatrix} = \begin{pmatrix} -1 & 0 & 0 \\ 0 & -1 & 0 \\ 0 & 0 & 1 \end{pmatrix}. \quad \text{(A10)}$$

The following relations are revealed from this rotation symmetry:

$$\begin{gathered} T_{xxx}=T_{yyy}=T_{xyy}=T_{yxx}=0, \\ T_{xxy}+T_{xyx}=T_{yxy}+T_{yyx}=0, \\ T_{zxz}+T_{zzx}=T_{zyz}+T_{zzy}=0. \end{gathered} \quad \text{(A11)}$$

The mirror planes σ_h and σ_d are dictated by the following matrices:

$$\sigma_h=\begin{pmatrix} -1 & 0 & 0 \\ 0 & 1 & 0 \\ 0 & 0 & 1 \end{pmatrix} \quad \sigma_d=\begin{pmatrix} 1 & 0 & 0 \\ 0 & -1 & 0 \\ 0 & 0 & 1 \end{pmatrix}. \quad \text{(A12)}$$

Applying the two mirror symmetries yields additional zero elements

$$T_{xyz}+T_{xzy}=T_{yxz}+T_{yzx}=0. \quad \text{(A13)}$$

As a result, only two nonzero terms, $T_{xxz}+T_{xzx}\equiv T_1$ and $T_{yyz}+T_{yzy}\equiv T_2$ are left, which give photocurrent

$$\begin{aligned} J_x^{CPDE} &= T_1 q_x(\vec{E}\times\vec{E}^*)_z, \\ J_y^{CPDE} &= T_2 q_y(\vec{E}\times\vec{E}^*)_z. \end{aligned} \quad \text{(A14)}$$

The photon wave vector $\vec{q}$ is given by

$$\begin{pmatrix} q_x \\ q_y \\ q_z \end{pmatrix} = \begin{pmatrix} -q\sin(\theta)\cos(\phi) \\ -q\sin(\theta)\sin(\phi) \\ -q\cos(\theta) \end{pmatrix}. \quad \text{(A15)}$$

Therefore, Eq. (A14) yields J^{CPDE} with the following incident angle dependence:

$$\begin{aligned} J_x^{CPDE} &\propto \sin(2\alpha)\sin(2\theta)\cos(\phi), \\ J_y^{CPDE} &\propto \sin(2\alpha)\sin(2\theta)\sin(\phi). \end{aligned} \quad \text{(A16)}$$

Although J^{CPDE} can be created at the surface with C_{2v} symmetry, the ϕ dependence shows that J^{CPDE} is strongest when the light is incident longitudinal to the channel, while experimentally HDPC in our devices is strongest when light is incident transverse to the channel. Therefore, we conclude HPDC observed in our devices is unlikely originated from CPDE.

[1] C. Zhang, Z. Ni, J. Zhang, X. Yuan, Y. Liu, Y. Zou, Z. Liao, Y. Du, A. Narayan, H. Zhang *et al.*, Ultrahigh conductivity in Weyl semimetal NbAs nanobelts, Nat. Mater. **18**, 482 (2019).

[2] H. Yi, Z. Wang, C. Chen, Y. Shi, Y. Feng, A. Liang, Z. Xie, S. He, J. He, Y. Peng *et al.*, Evidence of topological surface state in three-dimensional Dirac semimetal Cd_3As_2, Sci. Rep. **4**, 6106 (2014).

[3] P. J. Moll, N. L. Nair, T. Helm, A. C. Potter, I. Kimchi, A. Vishwanath, and J. G. Analytis, Transport evidence for Fermi-arc-mediated chirality transfer in the Dirac semimetal Cd_3As_2, Nature (London) **535**, 266 (2016).

[4] B.-C. Lin, S. Wang, A.-Q. Wang, Y. Li, R.-R. Li, K. Xia, D. Yu, and Z.-M. Liao, Electric control of Fermi arc spin transport in individual topological semimetal nanowires, Phys. Rev. Lett. **124**, 116802 (2020).

[5] W. Yu, D. Rademacher, N. Valdez, M. Rodriguez, T. Nenoff, and W. Pan, Evidence of decoupling of surface and bulk states in Dirac semimetal Cd_3As_2, Nanotechnology **33**, 415002 (2022).

[6] O. F. Shoron, T. Schumann, M. Goyal, D. A. Kealhofer, and S. Stemmer, Field-effect transistors with the three-dimensional Dirac semimetal cadmium arsenide, Appl. Phys. Lett. **115**, 062101 (2019).

[7] N. Li, C.-G. Chu, J.-J. Chen, A.-Q. Wang, Z.-B. Tan, Z.-C. Pan, Z.-H. Chen, D.-P. Yu, and Z.-M. Liao, Gate-switchable SQUID based on Dirac semimetal Cd_3As_2 nanowires, Phys. Rev. B **107**, 224513 (2023).

[8] O. F. Shoron, M. Goyal, B. Guo, D. A. Kealhofer, T. Schumann, and S. Stemmer, Prospects of terahertz transistors with the topological semimetal cadmium arsenide, Adv. Electron. Mater. **6**, 2000676 (2020).

[9] D. Pesin and A. H. MacDonald, Spintronics and pseudospintronics in graphene and topological insulators, Nat. Mater. **11**, 409 (2012).

[10] X. Peng, Y. Yang, R. R. Singh, S. Y. Savrasov, and D. Yu, Spin generation via bulk spin current in three-dimensional topological insulators, Nat. Commun. **7**, 10878 (2016).

[11] J. W. McIver, D. Hsieh, H. Steinberg, P. Jarillo-Herrero, and N. Gedik, Control over topological insulator photocurrents with light polarization, Nat. Nanotechnol. **7**, 96 (2012).

[12] Y. Pan, Q.-Z. Wang, A. L. Yeats, T. Pillsbury, T. C. Flanagan, A. Richardella, H. Zhang, D. D. Awschalom, C.-X. Liu, and N. Samarth, Helicity dependent photocurrent in electrically gated $(Bi_{1-x}Sb_x)_2Te_3$ thin films, Nat. Commun. **8**, 1037 (2017).

[13] D.-X. Qu, X. Che, X. Kou, L. Pan, J. Crowhurst, M. R. Armstrong, J. Dubois, K. L. Wang, and G. F. Chapline, Anomalous helicity-dependent photocurrent in the topological insulator $(Bi_{0.5}Sb_{0.5})_2Te_3$ on a GaAs substrate, Phys. Rev. B **97**, 045308 (2018).

[14] L. Yang, Z. Liu, Y. Sun, H. Peng, H. Yang, T. Zhang, B. Zhou, Y. Zhang, Y. Guo, M. Rahn *et al.*, Weyl semimetal phase in the non-centrosymmetric compound TaAs, Nat. Phys. **11**, 728 (2015).

[15] B. M. Wang, Y. Zhu, H. C. Travaglini, R. Sun, S. Y. Savrasov, W. Hahn, K. van Benthem, and D. Yu, Spatially dispersive helicity-dependent photocurrent in Dirac semimetal Cd_3As_2 nanobelts, Phys. Rev. B **108**, 165405 (2023).

[16] P. Schönherr and T. Hesjedal, Structural properties and growth mechanism of Cd_3As_2 nanowires, Appl. Phys. Lett. **106**, 013115 (2015).

[17] K. Zhang, H. Pan, M. Zhang, Z. Wei, M. Gao, F. Song, X. Wang, and R. Zhang, Controllable synthesis and magnetotransport properties of Cd_3As_2 Dirac semimetal nanostructures, RSC Adv. **7**, 17689 (2017).

[18] K. Park, M. Jung, D. Kim, J. R. Bayogan, J. H. Lee, S. J. An, J. Seo, J. Seo, J.-P. Ahn, and J. Park, Phase controlled growth of Cd_3As_2 nanowires and their negative photoconductivity, Nano Lett. **20**, 4939 (2020).

[19] J. Gao, A. Cupolillo, S. Nappini, F. Bondino, R. Edla, V. Fabio, R. Sankar, Y.-W. Zhang, G. Chiarello, and A. Politano, Surface reconstruction, oxidation mechanism, and stability of Cd_3As_2, Adv. Funct. Mater. **29**, 1900965 (2019).

[20] L.-X. Wang, C.-Z. Li, D.-P. Yu, and Z.-M. Liao, Aharonov–Bohm oscillations in Dirac semimetal Cd_3As_2 nanowires, Nat. Commun. **7**, 10769 (2016).

[21] N. Li, Z.-B. Tan, J.-J. Chen, T.-Y. Zhao, C.-G. Chu, A.-Q. Wang, Z.-C. Pan, D. Yu, and Z.-M. Liao, Gate modulation of anisotropic superconductivity in Al–Dirac semimetal Cd_3As_2 nanoplate–Al Josephson junctions, Supercond. Sci. Technol. **35**, 044003 (2022).

[22] Y. Yang, X. Peng, H.-S. Kim, T. Kim, S. Jeon, H. K. Kang, W. Choi, J. Song, Y.-J. Doh, and D. Yu, Hot carrier trapping induced negative photoconductance in InAs nanowires toward novel nonvolatile memory, Nano Lett. **15**, 5875 (2015).

[23] E. Baek, T. Rim, J. Schtt, C.-K. Baek, K. Kim, L. Baraban, and G. Cuniberti, Negative photoconductance in heavily doped Si nanowire field-effect transistors, Nano Lett. **17**, 6727 (2017).

[24] J. Jeong, N. Aetukuri, T. Graf, T. D. Schladt, M. G. Samant, and S. S. Parkin, Suppression of metal-insulator transition in VO_2 by electric field–induced oxygen vacancy formation, Science **339**, 1402 (2013).

[25] Y. Hou, R. Xiao, X. Tong, S. Dhuey, and D. Yu, *In situ* visualization of fast surface ion diffusion in vanadium dioxide nanowires, Nano Lett. **17**, 7702 (2017).

[26] J. Ye, S. Inoue, K. Kobayashi, Y. Kasahara, H. Yuan, H. Shimotani, and Y. Iwasa, Liquid-gated interface superconductivity on an atomically flat film, Nat. Mater. **9**, 125 (2010).

[27] Y. Liu, C. Zhang, X. Yuan, T. Lei, C. Wang, D. Di Sante, A. Narayan, L. He, S. Picozzi, S. Sanvito *et al.*, Gate-tunable quantum oscillations in ambipolar Cd_3As_2 thin films, NPG Asia Mater. **7**, e221 (2015).

[28] S. D. Ganichev and W. Prettl, Spin photocurrents in quantum wells, J. Phys.: Condens. Matter **15**, R935 (2003).

[29] C. Le and Y. Sun, Topology and symmetry of circular photogalvanic effect in the chiral multifold semimetals: a review, J. Phys.: Condens. Matter **33**, 503003 (2021).

[30] M. Glazov and S. Ganichev, High frequency electric field induced nonlinear effects in graphene, Phys. Rep. **535**, 101 (2014).

[31] L. Zhu, Z. Yao, Y. Huang, C. He, B. Quan, J. Li, C. Gu, X. Xu, and Z. Ren, Circular-photon-drag-effect-induced elliptically polarized terahertz emission from vertically grown graphene, Phys. Rev. Appl. **12**, 044063 (2019).

[32] J. Quereda, T. S. Ghiasi, J.-S. You, J. van den Brink, B. J. van Wees, and C. H. van der Wal, Symmetry regimes for circular photocurrents in monolayer $MoSe_2$, Nat. Commun. **9**, 3346 (2018).

[33] D. Fu, J. Zou, K. Wang, R. Zhang, D. Yu, and J. Wu, Electrothermal dynamics of semiconductor nanowires under local carrier modulation, Nano Lett. **11**, 3809 (2011).